PHYSICAL REVIEW D VOLUME 48, NUMBER 7 1 OCTOBER 1993

Analyzing power measurement of *pp* elastic scattering in the Coulomb-nuclear interference region with the 200-GeV/*c* polarized-proton beam at Fermilab

N. Akchurin, J. Langland, and Y. Onel
Department of Physics and Astronomy, University of Iowa, Iowa City, Iowa 52242

B. E. Bonner, M. D. Corcoran, J. Cranshaw, F. Nessi-Tedaldi,* M. Nessi,* C. Nguyen,† J. B. Roberts, J. Skeens, and J. L. White‡
T.W. Bonner Nuclear Laboratory, Rice University, Houston, Texas 77251

A. Bravar, R. Giacomich, A. Penzo, P. Schiavon, and A. Zanetti
Sezione di Trieste, Istituto Nazionale di Fisica Nucleare, Trieste, Italy

J. Bystricky, F. Lehar, A. de Lesquen, and L. van Rossum
DAPNIA-SPP, CEN-Saclay, F-91191 Gif-sur-Yvette Cedex, France

J. D. Cossairt and A. L. Read
Fermi National Accelerator Laboratory, Batavia, Illinois 60510

A. A. Derevschikov, Yu. A. Matulenko, A. P. Meschanin, S. B. Nurushev, D. I. Patalakha, V. L. Rykov, V. L. Solovyanov, and A. N. Vasiliev
Institute of High Energy Physics, Serpukhov, Russian Federation

D. P. Grosnick, D. A. Hill, M. Laghai, D. Lopiano, Y. Ohashi,§ T. Shima, H. Spinka, R. W. Stanek, D. G. Underwood, and A. Yokosawa
Argonne National Laboratory, Argonne, Illinois 60439

H. Funahashi, Y. Goto, K. Imai, Y. Itow, S. Makino, A. Masaike, K. Miyake, T. Nagamine,‖ N. Saito, and S. Yamashita
Department of Physics, Kyoto University, Kyoto 606, Japan

K. Iwatani
Hiroshima University, Higashi-Hiroshima 724, Japan

K. Kuroda and A. Michalowicz
Laboratoire de Physique des Particules, Boite Postale 909, 74017 Annecy-le-Vieux, France

F. C. Luehring¶ and D. H. Miller
Physics Department, Northwestern University, Evanston, Illinois 60201

T. Maki
University of Occupational and Environmental Health, Kita-Kyushu 807, Japan

G. Pauletta
Istituto di Fisica, University of Udine, I-33100 Udine, Italy

G. F. Rappazzo and G. Salvato
Dipartimento di Fisica, Università di Messina and Gruppo Collegato INFN-Messina, I-98100, Messina, Italy

R. Takashima
Kyoto University of Education, Kyoto 612, Japan

F. Takeutchi
Kyoto-Sangyo University, Kyoto 612, Japan

(Fermilab E581/704 Collaboration)

(Received 6 April 1993)

0556-2821/93/48(7)/3026(11)/$06.00

The analyzing power A_N of proton-proton elastic scattering in the Coulomb-nuclear interference region has been measured using the 200-GeV/c Fermilab polarized proton beam. A theoretically predicted interference between the hadronic non-spin-flip amplitude and the electromagnetic spin-flip amplitude is shown for the first time to be present at high energies in the region of 1.5×10^{-3} to $5.0 \times 10^{-2} (\mathrm{GeV}/c)^2$ four-momentum transfer squared, and our results are analyzed in connection with theoretical calculations. In addition, the role of possible contributions of the hadronic spin-flip amplitude is discussed.

PACS number(s): 13.88.+e, 13.85.Dz, 29.25.Pj, 29.27.Hj

I. INTRODUCTION

It is commonly believed that polarization in elastic scattering would vanish at high energy where the amplitudes are eventually dominated by diffraction, parametrized in terms of Pomeron exchange having no spin-flip terms. However Schwinger [1] pointed out that large polarization of fast neutrons is possible by the spin-orbit interaction arising from the motion of the neutron magnetic moment in the nuclear Coulomb field at very small scattering angles due to the long-range nature of the electromagnetic interactions. Several authors [2–5] also showed that a small but considerable asymmetry was expected in high-energy *pp* elastic scattering at small four-momentum transfer squared $|t| \approx 0.003$ $(\mathrm{GeV}/c)^2$ which arises from the interference between the hadronic nonflip and the electromagnetic spin-flip amplitude. In terms of helicity amplitudes, this is expressed as [6,7]

$$A_N \frac{d\sigma}{dt} = -\mathrm{Im}\{(\phi_1 + \phi_2 + \phi_3 - \phi_4)\,\phi_5{}^*\} \;, \tag{1}$$

where $\frac{d\sigma}{dt}$ is the spin-averaged differential cross section:

$$\frac{d\sigma}{dt} = \frac{\pi}{2k^2}\left[|\phi_1|^2 + |\phi_2|^2 + |\phi_3|^2 + |\phi_4|^2 + 4|\phi_5|^2\right] \;. \tag{2}$$

If the higher-order electromagnetic terms are neglected, and under the hypothesis of the additivity of the hadronic and electromagnetic amplitudes, ($\phi_i = \phi_i{}^h + \phi_i{}^e$), the differential cross section can be expressed in the Coulomb-nuclear interference (CNI) region as

$$\frac{d\sigma}{dt} = \frac{d\sigma^e}{dt} + \frac{d\sigma^h}{dt} + \frac{d\sigma^i}{dt} \;, \tag{3}$$

where the superscripts indicate electromagnetic, hadronic, and interference contributions to the differential cross section; these are usually parametrized as

$$\frac{d\sigma}{dt} = \frac{4\pi\alpha^2}{t^2} + \frac{\sigma_{\mathrm{tot}}^2}{16\pi}(1+\rho^2)e^{bt} - \frac{e^{\frac{bt}{2}}}{t}\alpha\sigma_{\mathrm{tot}}(\sin 2\delta + \rho\cos 2\delta) \;, \tag{4}$$

where α is the fine structure constant, ρ is the ratio of the real to the imaginary parts of the hadronic scattering amplitude at $t = 0$, δ is Bethe's phase shift $[\delta = -(\ln|t| + \ln b + 0.577)\frac{\alpha}{\beta}]$, b is the nuclear slope parameter, and β is the velocity of the incident proton.

The electromagnetic amplitudes are written in the one-photon exchange approximation, keeping the leading terms only at high energy and small momentum transfer $|t|$ $(s \gg m^2 \gg |t|)$:

$$\phi_1^e = \phi_3^e \approx \frac{\alpha\sqrt{s}}{t}, \tag{5}$$

$$\phi_2^e = -\phi_4^e \approx \frac{\alpha\sqrt{s}}{4m^2}\,(\mu-1)^2 \qquad (\mu = 2.79), \tag{6}$$

$$\phi_5^e = -\frac{\alpha\sqrt{s}}{|t|^{1/2}}\frac{\mu-1}{2m}. \tag{7}$$

The contribution of the different components to the total asymmetry is written as

$$A_N\frac{d\sigma}{dt} = \left(A_N\frac{d\sigma}{dt}\right)^e + \left(A_N\frac{d\sigma}{dt}\right)^h + \left(A_N\frac{d\sigma}{dt}\right)^i . \tag{8}$$

In Eq. (3) the interference term originates from the nuclear nonflip amplitude and the Coulombic charge-charge interaction. In Eq. (8), however, the interference comes from the nuclear nonflip amplitude and the charge-magnetic moment interaction which gives an electromagnetic spin-flip amplitude. The major contribution to the asymmetry comes from the interference of ϕ_1^h and ϕ_3^h (nonflip) with ϕ_5^e (single-flip) amplitudes. The imaginary part of the hadronic amplitudes ϕ_1^h and ϕ_3^h can be calculated by the optical theorem, using the total cross section σ_{tot}:

$$\mathrm{Im}(\phi_1^h + \phi_3^h) = \frac{1}{4\pi}[s(s-4m^2)]^{1/2}\sigma_{\mathrm{tot}} \;, \tag{9}$$

where s is the center-of-mass energy squared and m is the proton mass.

Assuming a zero electromagnetic A_N^e (single-photon

---

*Permanent address: CERN, CH-1211 Geneva 23, Switzerland.

†Permanent address: University of Texas, Austin, TX 78712.

‡Permanent address: American University, Washington, D.C. 20016.

§Permanent address: Institute of Physical and Chemical Research, Saitama, Japan.

‖Permanent address: Stanford Linear Accelerator Center, Stanford, CA 94305.

¶Permanent address: Indiana University, Bloomington, IN 47405.

exchange), the asymmetry in the Coulomb-nuclear interference region is written as [2]

$$A_N(t) = A_N^h(t)\,\frac{1}{1+\left(\frac{d\sigma}{dt}/\frac{d\sigma^h}{dt}\right)} + A_N^i(t), \qquad (10)$$

$$A_N^i(t) = A_N^i(t_p)\frac{4z^{3/2}}{3z^2+1}, \qquad (11)$$

where $z = t/t_p$ and $t_p = \sqrt{3}(8\pi\alpha/\sigma_{\text{tot}}) \approx 3.12 \times 10^{-3}$ $(\text{GeV}/c)^2$. The maximum interference asymmetry is

$$A_N^i(t_p) \approx \frac{\sqrt{3}}{4}(\mu-1)\frac{\sqrt{t_p}}{m} \approx 0.046, \qquad (12)$$

where μ is the total magnetic moment of proton and m is the proton's mass. $A_N^h(t)$ at small $|t|$ values, on the other hand, appears to behave like [8]

$$A_N^h(t) \approx \sqrt{\frac{t}{s}} \qquad (13)$$

and, accordingly, the interference term should dominate for $|t| \leq 6 \times 10^{-3}$ $(\text{GeV}/c)^2$ at energies higher than 50 GeV.

Previous measurements with polarized targets could not access such a small $-t$ region because the recoil would be reabsorbed in the target, thereby making the kinematical determination of elastic-scattering events on the polarized free protons in the target impossible. By making use of a polarized beam and a recoil sensitive scintillator target we were able to observe polarization effects in the CNI region for the first time at high energies.

It should be noted that in the past high resolution forward spectrometers [9,10] and/or gaseous targets with recoil detection [11] were employed for the measurements in the CNI region at high energies with an unpolarized beam and target; on the other hand, for colliding beams the experimental problem is the detection of the scattered particles very close to the circulating beam [12,13].

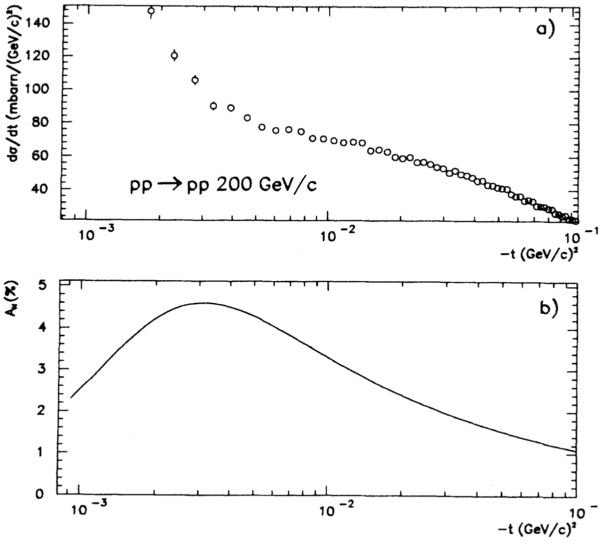

FIG. 1. (a) The $pp \to pp$ differential cross-section measurement at 200 GeV/c [9] and (b) proton analyzing power as a function of $-t$ for the CNI process. The $|t|$ dependence of the differential cross section and the ratio of imaginary to real parts of the forward amplitudes ρ are neglected.

Figure 1(a) shows the differential cross-section measurement at 200 GeV/c [9], and Fig. 1(b) the theoretical prediction for the CNI analyzing power A_N as a function of the four-momentum transfer squared [2]. Although the maximum polarization is only ~4.6%, the average integrated cross section for $0.004 \leq t \leq 0.04$ $(\text{GeV}/c)^2$ is relatively large, ~3.10 mb. This makes such an interference measurement possible and also suitable for applications as a high-energy polarimeter.

If, however, the hadronic spin-flip amplitude is other than zero, the asymmetry predictions change. This could be the case, for instance, if the proton wave function contains a dynamically enhanced diquark thus resulting in a spin-flip term appearing [14]. The question of spin-flip contributions to diffraction scattering has often been debated in the literature based on previous polarization measurements at higher $-t$ values and at 100 – 300 GeV/c [15–18], that indicate a flattening of the asymmetry at high energies.

II. EXPERIMENTAL SETUP

Figure 2 shows the experimental setup, including Fig. 2(a) the schematic layout of the polarized ($p/\bar{p}$) beam line at Fermilab and Fig. 2(b) the top view of the CNI apparatus. Polarized protons are produced in the parity-nonconserving decays of Λ hyperons. The incoming 800-GeV/c primary proton beam strikes a beryllium target and creates unpolarized Λ's. In order to maximize the Λ intensity, the beam-line acceptance is centered around 0° production angle. These Λ hyperons on the average are unpolarized. In the unpolarized Λ rest frame, the decay $\Lambda \to p+\pi^-$ occurs isotropically and the decay-proton polarization is 64% with the spin direction along the proton momentum (for details see [19]). The 200-GeV/c polarized protons strike the active targets after their spins are rotated from horizontal to vertical by spin-rotation magnets. Beam hodoscopes, beam chambers, before and after the spin-rotation magnets, and a pair of multistrip silicon detectors before the targets track the incident beam. The scattered track, after the active targets, is detected by a series of multiwire proportional chambers (MWPC's) up to the analyzing magnet, which is located at z = 15.04 m. The track deflected by the analyzing magnet (BM-109) is measured by yet another set of MWPC's and a Gray-Code (GC) hodoscope (z = 46.20 m). In order to center the deflected beam in the middle of the GC hodoscope, the GC was mounted on a remote-controlled movable pedestal. The deflection from the undeflected beam axis was about 12.98 cm at the GC when the magnet was operating at 2500 A.

The multiscintillator target (MST) ensemble consisted of six *trans*-stilbene crystals (diphenyl-ethlylene, $C_{14}H_{12}$) which have good pulse-shape discrimination (PSD) characteristics, and each target element was viewed by an

XP2020 photomultiplier tube (see Table I).

For scattering events on the H atoms of the scintillator, the energy of the recoil proton ranges from a few MeV up to 24 MeV and the range of the recoil proton goes as high as 7 mm in *trans*-stilbene. Since these protons recoil close to 90° with respect to the beam axis, the target dimensions are chosen to be 3–4 cm in diameter and only a few millimeters in thickness.

The targets were aligned on an optical bench with respect to the beam line and oriented normally to the beam direction in order to minimize the amount of energy deposited by through-going (minimally ionizing) beam and scattered protons and to maximize the response to protons that recoil (heavily ionizing) at angles of about 90°. The difference in pulse amplitudes between the through-going and the recoil proton, which deposits all of its energy in the target, is the principal idea of the discrimination between the two cases. This constitutes the first selection criterium in the first level trigger. There are, however, practical difficulties associated with this idea. The energy distribution of the through-going particles obeys an asymmetric Landau distribution. This distribution has a long tail in the higher-energy end; extending somewhat into the energy range where energy distribution of the recoil protons starts. In order to minimize this effect, and to provide a sharper criterium for triggering over threshold, we chose a scintillating target that possesses PSD characteristics; i.e., the time dependence of luminescence depends on the ionization density and therefore on the energy of the particles. The slow recoil protons produce, in the MST *trans*-stilbene crystals, pulses that have on the average a longer duration than that of the through-going beam particles.

TABLE I. Dimensions and surveyed and reconstructed positions for each target along the beam line. The mean z-vertex position and the standard deviation values are Gaussian-fitted values.

Target No.	Thickness (mm)	z vertex[a] (cm)	z vertex[b] (cm)	σ (cm)
1	2.0	−60.1	−59.5	24.7
2	2.0	−20.1	−15.6	32.0
3	3.0	19.9	21.5	32.8
4	3.0	39.9	41.5	28.8
5	5.0	59.9	60.0	30.6
6	6.2	79.9	79.9	28.8

[a] Surveyed positions.
[b] Reconstructed positions.

Figure 3 schematically represents the timing characteristics of a scintillating material with PSD properties. The total light output from the crystal can be parametrized as a sum of the fast and slow components, i.e.,

$$L(t) = L_f \exp(-t/\tau_f) + L_s \exp(-t/\tau_s). \qquad (14)$$

τ_f and τ_s are the decay-time constants and L_f and L_s are the fitted coefficients for the fast and slow components, respectively. The fast decay-time constant τ_f is measured to be 4–6 ns and the slow decay-time constant is ~ 275 ns

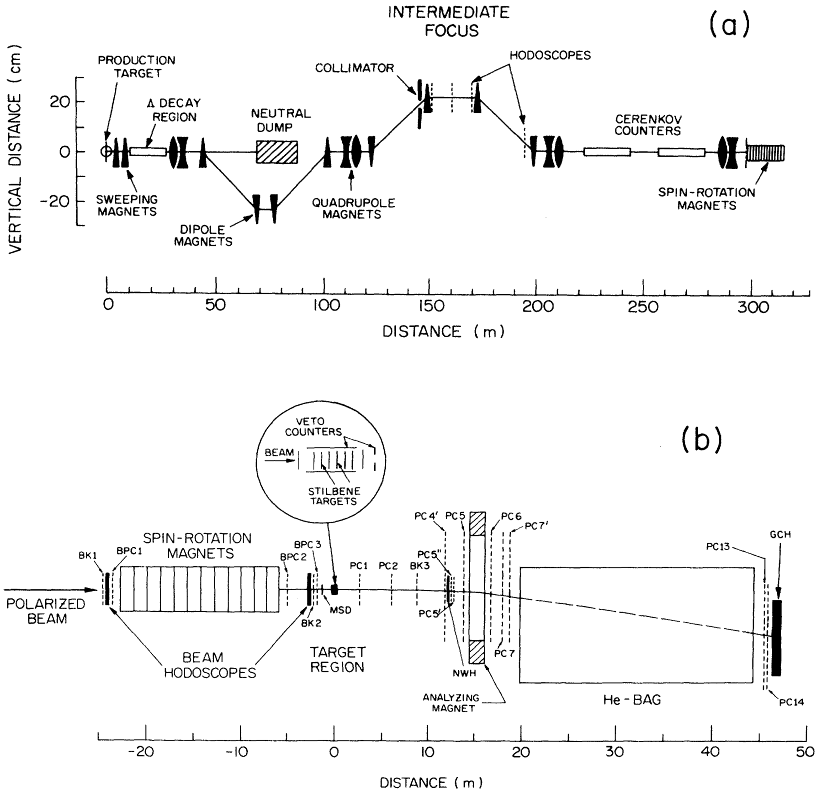

FIG. 2. (a) The side view of the secondary beam-line elements. The secondary beam-line consists of production target, neutral particle dump, adjustable collimator, beam tagging region, and Cherenkov counters before the spin rotating magnets and the experimental target(s). For more details see [19]; (b) top-view layout of the CNI polarimeter. The dimensions transverse to the beam are not to scale.

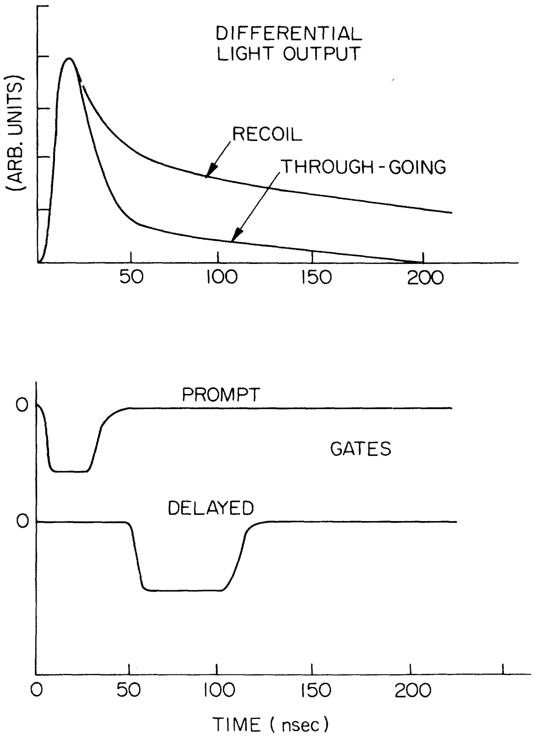

FIG. 3. PSD characteristics of *trans*-stilbene. The recoil particles generate a pulse with longer tails compared to the minimally ionizing particles. By choosing appropriate gates, this characteristic of the crystal is exploited to distinguish recoils from beam particles.

[20,21]. By selecting the fast and slow parts of the pulses from the *trans*-stilbene crystals with prompt and delayed gates set according to the decay times, a simple PSD trigger can be constructed.

The entire target ensemble was surrounded by 11 lead-scintillator sandwich veto counters to eliminate all scattering and production processes, except those close to the beam. The most effective veto counter was the forward one positioned normally to the beam direction, with a 4.7-cm hole in the middle of the counter, which was centered around the beam.

The momentum transfer $|t|$ from the incident particle to the scattered proton is measured by reconstructing the track of the scattered proton. The kinetic energy of the recoil proton can be expressed as $T = |t|/2m$. Thus, it is possible to make a correlation between the two experimental and independently determined quantities, i.e., the kinematically measured $|t|$ values and the pulse amplitude recorded for the same event. This criterion, in principle, provides a tool for carbon background suppression since $T_{\text{carbon}} \approx \frac{1}{12} T_{\text{hydrogen}}$ for the same scattering angle.

For this measurement, 42 planes of multiwire proportional chambers and 2 orthogonal planes of multistrip silicon detectors (MSD's) were used. The MSD's (3 cm × 3 cm) had 100-μm strips and were located before the targets at $z = -171.8$ cm.

An analyzing magnet was used to analyze the momentum of the particles. It was centered around $z = 15.04$ m and operated at 2500 A during data taking. The magnet gap is 24 in.×21 in. in the x and y directions, respectively. The magnetic field is effectively flat at 13.78 KG in the central region. The momentum kick is about ~ 0.4 GeV/c.

The Gray Code (GC) hodoscope consists of two identical arrays with vertical and horizontal scintillator strips, determining the x and y coordinates of the transmitted particles, respectively. It is segmented into $2^5 = 32$ bins, each 5 mm wide. Each array is subdivided into *direct* and *inverse* sections, and each is viewed by a set of five photomultiplier tubes (PMT's) (for details see [22]). Two counters (16 cm × 16 cm) are placed immediately before and after the hodoscope and are used in coincidence with the hodoscope elements.

III. TRIGGER

The trigger for the CNI polarimeter consists of two major parts. The first part generates a good target (GT*) signal by exploiting the PSD characteristics of the active *trans*-stilbene targets whenever there is a recoil candidate in one of the six targets. The second part, initiated by the GT* signal, checks the scattering and azimuthal angles of the event by using the GC and makes a decision based on the information loaded on memory logic units (MLU's).

Figure 4 shows the simplified scheme of the PSD part;

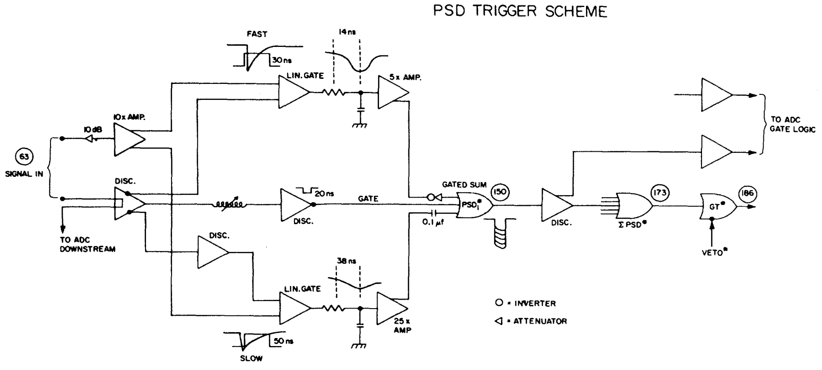

FIG. 4. Simplified PSD trigger used in this measurement. The times of propagation of signals in nanoseconds are indicated by the numbers in circles.

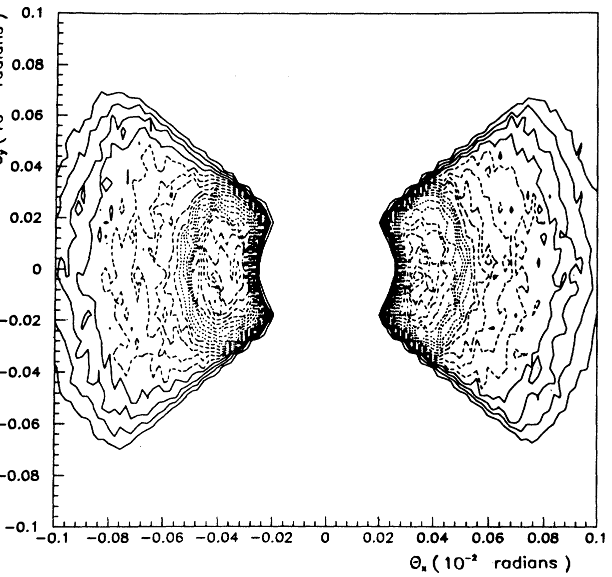

FIG. 5. The *butterfly* cut as observed at GC. The events in the central part (beam), upper and lower quadrants are rejected at the trigger level.

the pulse is separated into fast (F) and slow (S) parts by means of linear gates and a trigger is generated whenever the ratio S/F exceeds a given threshold. It typically takes 185 ns to make a PSD decision. The total and the slow components of the pulses from each target crystal are read also by analogue-to-digital converters (ADC's) (130 ns gate width). If there is a good event, i.e., master trigger, the ADC's are read and cleared.

The MLU logic is designed such that it projects the undeflected beam track onto the GC and checks if the event meets the scattering requirements for the forward scattering angle θ_s and the azimuthal angle ϕ. MLU's are loaded with a *butterfly* cut (Fig. 5) to eliminate the up and down scattered particles and a 1.1 cm × 1.1 cm square is cut out in the center to eliminate the straight-through beam particles, thus accepting only particles that scatter left and right of the beam.

The diffuseness of the MLU cuts has an impact in the very low $-t$ region in terms of background. The events that scatter at very small angles are sensitive to the sharpness of the cuts. The border effects of the GC also contribute to this in a lesser degree since the inconsistent events are omitted by the coding of the hodoscope at the trigger level.

IV. DATA ANALYSIS

There are two major parts to the apparatus of the Coulomb-nuclear interference measurement, i.e., the forward spectrometer and the active *trans*-stilbene targets. The correlation between the scattering angle measured by the forward spectrometer and the pulse amplitude from the recoil protons in the active *trans*-stilbene targets constitutes the primary criterion in separating the elastic *pp* events from a number of different backgrounds.

The reconstructed tracks determine four of the critical parameters of the measurement, i.e., vertex position, scattering angle θ_s, azimuthal angle ϕ, and momentum of the scattered particle. In the off-line vertex analysis, the hodoscopes upstream of the target area and the GC are mainly used to define a road in which the tracks are reconstructed. This procedure saves significant time in computing. The reconstruction is done in three different stages; the incident track before the targets, the scattered track after the targets and the deflected track after the analyzing magnet. The track is reconstructed for each segment and at the intersection points (target and the analyzing magnet) the distance between the tracks is minimized. The maximum allowed distance is 2 mm in both the x and y directions. At the target and at the analyzing magnet locations, the tracks are joined when the χ^2 values are acceptable.

The CNI trigger requires that the beam interacts only in one of the targets, and until the event is fully processed the data acquisition system is latched. In this way the reconstruction of the z-vertex distribution for each target is possible. All the multiple-track events are also rejected. The standard deviation for the z-vertex distribution for individual targets range from 24.7 to 32.8 cm and the absolute value of the difference between the mean reconstructed z vertex and the surveyed target position ranges from 0.1 to 4.5 cm (Table I).

The momentum measurement of the incident protons with the forward spectrometer and the spectrometer at the tagging region in the intermediate focus of the beam agree within a few percent. The beam momentum spread is about ±9% and the mean momentum is 200 GeV/c.

The momentum spread of the beam is further dispersed by the analyzing magnet. This smears the distribution of events detected at GC, thereby directly effecting the low $-t$ cut in the trigger. Momentum correction for each event using the tagged beam momentum at the level of MLU's was employed in the trigger. On the other hand, the analyzing magnet reduces the background due to low-energy charged particles at the level of the trigger.

The fractional accuracy of the analyzing magnet is given by

$$\frac{\Delta p}{p} = 0.003\frac{p\Delta\theta_B}{BL} \tag{15}$$

and it is estimated to be about 1%. The momentum p is 200 GeV/c, the accuracy of the bending angle $\Delta\theta_B$ is about 0.042 mrad and BL is 2.52-T meters.

A. Selection of *pp* elastic events

The correlation between the four-momentum transfer squared $|t|$ (or the forward scattering angle θ_s) and the ADC counts of pulse amplitudes is used in identifying the elastic events. The elastic events present themselves as a distinct diagonal band on the $|t|$ vs ADC scatter plot. Scattering from the carbon nuclei and the straight-through events are observed as a horizontal band. Figure 6 shows this correlation between $|t|$ and the slow component of the ADC for target 1.

There are processes other than elastic *pp* scattering that take place when a proton strikes a target. Scattering from the carbon nuclei constitutes one of the sources of background. Straight-through particles also obscure the elastic *pp* events, especially in the lowest $|t|$ region. In addition, a broad distribution of quasielastic events contributes to the background. In order to extract the pure *pp* elastic events from the background, three different criteria are applied to the data set.

(1) *A priori*, two parallel diagonal cuts, above and below the elastic-event band, are applied to eliminate most of the uncorrelated and quasielastic events.

(2) A z-vertex cut, $|z_{\text{reconstructed}} - z_{\text{surveyed}}| \tan\theta_s < M\sigma$, where $1.65 \le M \le 2.2$ and σ is the standard deviation of the $(z_{\text{reconstructed}} - z_{\text{surveyed}}) \tan\theta_s$ distribution, constrains the events that come from a given target.

(3) Much like the case above, another constraint is constructed for the four-momentum transfer squared. If $|t_{\text{measured}} - t_{\text{expected}}| > \Delta$, where $0.009\,(\text{GeV}/c)^2 \le \Delta \le 0.01\,(\text{GeV}/c)^2$, then the event is rejected. t_{expected} is deduced from the recoil energy as described below.

The ADC (slow component) counts vs $-t$ for target 1 are shown in Fig. 6(b) after the z vertex cut is applied. In general, the background events are seen only in the lowest ADC channels. These events are mostly due to carbon scattering, minimally ionizing through-going beam particles with large multiple scattering and uncorrelated particles that are accepted by the trigger.

If one makes a binning of the $|t|$ vs ADC correlation, in equal $|t|$ intervals $[\Delta t = 0.0025(\text{GeV}/c)^2]$, the projection of the events onto the ADC axis exhibits the distributions that are obeyed by each specific type of event (see Fig. 7). The through-going particles show a Landau-tail distribution cut at the low side by our trigger threshold, whereas the *pp* recoil events obey Gaussian statistics. The sum of the asymmetric tail of the Landau distribution and a free varying Gaussian distribution for the elastic *pp* events is fitted to the ADC spectra. The most probable energy and the mean energy deposition of through-going protons are calculated from the Bethe-Bloch equation and used to fix the Landau distribution in energy. The most probable energy loss for the targets of different thickness ranges between 0.3 and 0.9 MeV, whereas the mean energy loss ranges from 0.6 to 1.8 MeV [23]. As $|t|$ values increase, the Gaussian distribution separates from the background events, enabling us to make a correlation beween the $|t|$ values and expected ADC counts per hit. The central peaks of the Gaussian distribution, in the relatively background-free momentum-transfer region, can be linearly fitted to form a correlation between the expected $|t|$ and ADC values. Based upon this criterion, it is possible to further restrict the $|t|$ vs ADC correlation. From this linear fit, t_{expected} values are calculated for each measured ADC count. The first few bins are omitted from the fit so as not to produce bias by the events that are at the very low $-t$ region which is most contaminated by background. Consequently, comparison of the expected and the measured $-t$ values is possible. As mentioned earlier, this criterion is used to constrain the $-t$ distribution further, in particular at low $-t$.

The quasielastic scattering and recoil protons that escape from the targets present a broader spectrum of lower level background in a larger $|t|$ range. The inelastic events are principally vetoed by the target veto counters that surround the target assembly.

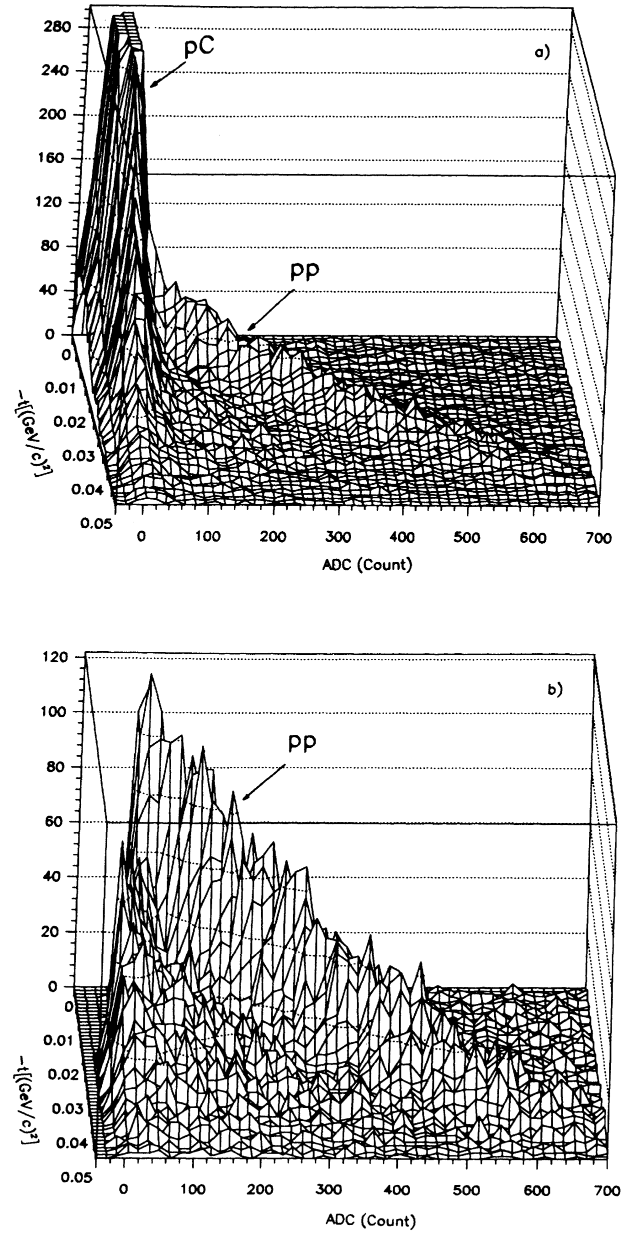

FIG. 6. The correlation between the four-momentum transfer squared $-t$ and the ADC slow component for target 1. The x axis represents the ADC counts; the y axis is the four-momentum transfer squared in $(\text{GeV}/c)^2$; and the z axis represents the number of events. Plots shown are (a) before the elastic *pp* event selection; (b) after the z vertex cut as described in Sec. IV A. The diagonal band of events is due to elastic *pp* scattering. The background is observed as the high horizontal band.

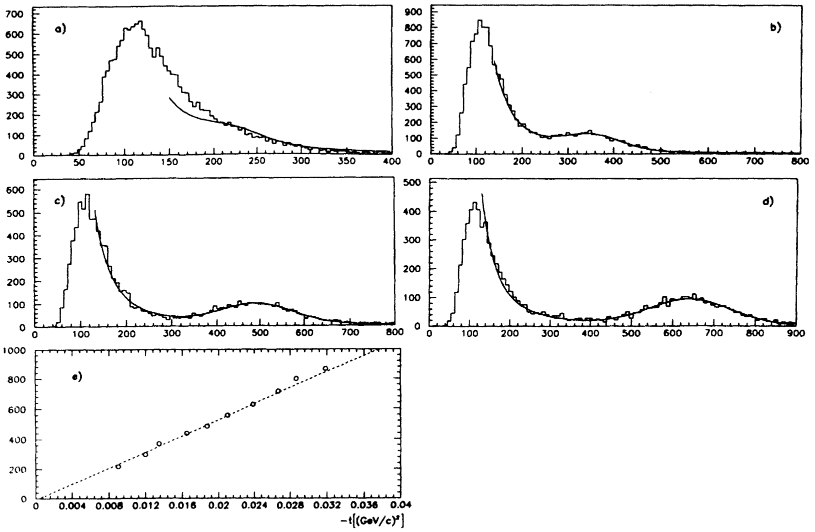

FIG. 7. The projection of slow component ADC values as a function of $-t$ bins where each plot corresponds to $\Delta t = 0.0025\,(\mathrm{GeV}/c)^2$. In the case of the lower t range the background is dominant and described by a Landau distribution and as the $-t$ values increase the elastic *pp* events separate from the background and exhibit a Gaussian distribution. The plots represent the ADC spectra for the $-t$ bins of (a) $0.0075 \leq -t \leq 0.0100\,(\mathrm{GeV}/c)^2$; (b) $0.0125 \leq -t \leq 0.0150\,(\mathrm{GeV}/c)^2$; (c) $0.0175 \leq -t \leq (\mathrm{GeV}/c)^2$; (d) $0.0225 \leq -t \leq 0.0250\,(\mathrm{GeV}/c)^2$; and (e) shows the scaling of the mean of the *pp* elastic peak with the four-momentum transfer squared.

The factors that determine the precision of the forward spectrometer are the multiple scattering of the forward particles, the measurement accuracy of the wire chambers and the uniformity (momentum kick) of the analyzing magnet.

The multiple-scattering effects are due to the elastic Coulomb interactions of the forward particles with the material in the beam. This can be calculated as follows:

$$\Delta\theta_{\mathrm{MS}} = \frac{14.1}{p}\sqrt{L/L_R}(1 + 1/9\log_{10}L/L_R)\ , \qquad (16)$$

where p is the particle momentum in GeV/c and $\Delta\theta_{\mathrm{MS}}$ is in milliradians. L is the length of the material in the beam and L_R is the radiation length of the material. Since in Coulomb-nuclear interference the angles of scattering are in the order of fractions of milliradians, it is important to minimize the mass in the beam. We had He bags between detector elements to minimize multiple scattering. The total amount of material in the beam for our measurement resulted in $\Delta\theta_{\mathrm{MS}} \approx 0.021$ mrad.

The measurement error can be estimated from the position resolution of the MWPC, $\sigma = 0.289S$ where S is MWPC wire spacing in mm. The measurement error is about 0.033 mrad for our geometrical setup.

The multiple scattering of the events from the material in the beam contribute to the overall broadening of the $-t$ distribution. The average scattering angle for the first $-t$ bin is about 0.33 mrad. Thus, this particular $-t$ bin is more sensitive to the multiple scattering of the events. We applied a tighter cut in the z vertex in order to reject through-going particles more effectively, which could dilute the observed asymmetry in the lowest $-t$ bin.

V. CALCULATION OF ASYMMETRIES

In extracting the analyzing power A_N from the measured count rates there are several ways of calculating the *raw* asymmetries ϵ as a function of the various parameters defining the scattering event and the beam spin state.

(1) Left-right scattering: The apparatus is (in principle) left-right symmetric with respect to the beam. The azimuthal angle ϕ is measured by the spectrometer. At the trigger level two regions are defined ($L \equiv -\Phi < \phi < \Phi$ and $R \equiv \pi - \Phi < \phi < \pi + \Phi$), for all of the scattering angle θ_s accepted and $\Phi \approx \pi/4$.

(2) Polarization tagging: The beam contains both positive and negative polarization states in seven bins $P_i = (i = 1, ..., 7)$ from -65% to +65%. Omitting the central bin, $i = 4$ (average zero polarization state, $\langle P_4 \rangle = 0$) used for control purposes only, we define negative $P_-, P < 0$ ($i = 1, 2, 3$) and positive $P_+, P > 0$ ($i = 5, 6, 7$) polarization states of the beam. The polarization bins are defined such that $i = 1\,(-65\% : -55\%), i = 2\,(-55\% : -45\%), i = 3\,(-45\% : -35\%), i = 4\,(-35\% : +35\%), i = 5\,(+35\% : +45\%), i = 6\,(+45\% : +55\%)$ and $i = 7\,(+55\% : +65\%)$.

(3) Snake magnet state: Snake magnets reverse the spin direction every 10 spills (~ six times per hour). This reversal of spin direction is used to eliminate the systematic errors. The state of the snake system is labeled according to the orientation of the polarization state from tagging at the target.

For each $|t|$ bin, the number of events as a function of the above three parameters is defined as $N = N(L/R, +/-, \uparrow\ /\ \downarrow)$ = (left/right, polarization state, snake state). For example,

$$N(L,+,\uparrow) = N(+,\uparrow)\alpha(L)\int_{-\Phi}^{\Phi} d\phi \int_{\theta-\delta\theta/2}^{\theta+\delta\theta/2} \frac{d\sigma}{d\Omega}\sin\theta d\theta\,[1 + A_N(\theta)P_+\cos\phi], \qquad (17)$$

$$N(R,-,\uparrow) = N(-,\uparrow)\alpha(R)\int_{-\Phi}^{\Phi} d\phi \int_{\theta-\delta\theta/2}^{\theta+\delta\theta/2} \frac{d\sigma}{d\Omega}\sin\theta d\theta\,[1 + A_N(\theta)P_- \cos\phi], \tag{18}$$

$$N(L,-,\downarrow) = N(-,\downarrow)\alpha(L)\int_{-\Phi}^{\Phi} d\phi \int_{\theta-\delta\theta/2}^{\theta+\delta\theta/2} \frac{d\sigma}{d\Omega}\sin\theta d\theta\,[1 + A_N(\theta)P_- \cos\phi], \tag{19}$$

$$N(R,+,\downarrow) = N(+,\downarrow)\alpha(R)\int_{-\Phi}^{\Phi} d\phi \int_{\theta-\delta\theta/2}^{\theta+\delta\theta/2} \frac{d\sigma}{d\Omega}\sin\theta d\theta\,[1 + A_N(\theta)P_+ \cos\phi]. \tag{20}$$

The azimuthal angle ϕ is integrated between the maximum and the minimum of the ϕ acceptance (see Fig. 5). $N(+,\uparrow)$, etc., refer to the beam flux for each (tagging and snake) state and $\alpha(L)$, etc., represents the weighting factor for the left scattering (including efficiencies and acceptances) for the considered $|t|$ bin. The other four states are expressed in a similar way with a negative sign in front of A_N.

We define the following rates in the left and right regions according to the polarization state at the target:

$$L^+ = [N(L,+,\uparrow)N(L,-,\downarrow)]^{1/2} \quad \text{and} \quad R^- = [N(R,+,\downarrow)N(R,-,\uparrow)]^{1/2}\ , \tag{21}$$

$$R^+ = [N(R,+,\uparrow)N(R,-,\downarrow)]^{1/2} \quad \text{and} \quad L^- = [N(L,+,\downarrow)N(L,-,\uparrow)]^{1/2}\ . \tag{22}$$

By using the geometrical mean, all the normalization coefficients are factored out and are automatically canceled when the asymmetry is calculated as

$$\begin{aligned} \epsilon &= \frac{\sqrt{L^+R^-} - \sqrt{L^-R^+}}{\sqrt{L^+R^-} + \sqrt{L^-R^-}} \\ &= \frac{N(+)P_+ + N(-)P_-}{N(+) + N(-)} \left(\frac{\sin\Phi}{\Phi}\right) \frac{\int A_N(\theta)\frac{d\sigma}{d\Omega}\sin\theta d\theta}{\int \frac{d\sigma}{d\Omega}\sin\theta d\theta}, \end{aligned} \tag{23}$$

where on the right side of Eq. (23), the first multiplicative term is the average beam polarization, the second term is the azimuthal detector acceptance, and the last term is the *pp* analyzing power. The value of A_N in the $|t|$ bin considered is therefore

$$A_N(t) = \frac{\Phi}{\sin\Phi}\,\frac{\epsilon}{P_{\text{beam}}}. \tag{24}$$

The approximate statistical error can be estimated as

$$\Delta\epsilon \approx \frac{1-\epsilon^2}{\sqrt{N_{\text{tot}}}}. \tag{25}$$

The systematic effects are estimated by considering $\epsilon(\langle P_{\text{beam}}\rangle = 0)$, using the central bin of the tagging states (Table II) and by the *fake* asymmetries. Therefore, six other asymmetries are calculated as a measure of control of the apparatus and a double check of the results. These are $\epsilon_{L/R}, \epsilon_{\uparrow/\downarrow}$, and $\epsilon_{+/-}$. They are defined as

$$\epsilon_{L/R} = \frac{\sqrt{N(L/R,+,\uparrow)N(L/R,-,\downarrow)} - \sqrt{N(L/R,+,\downarrow)N(L/R,-,\uparrow)}}{\sqrt{N(L/R,+,\uparrow)N(L/R,-,\downarrow)} + \sqrt{N(L/R,+,\downarrow)N(L/R,-,\uparrow)}}, \tag{26}$$

TABLE II. Results of the CNI measurement. The last column is the raw asymmetry measured with the part of the beam where the average beam polarization is zero.

$-t$ range $(\text{GeV}/c)^2$	$\langle -t\rangle$ $(\text{GeV}/c)^2$	N Events	A_N (%)	Raw asym. $\langle P_b\rangle = 0$ (%)
$1.50\times10^{-3} - 4.00\times10^{-3}$	2.88×10^{-3}	5695	4.46 ± 3.16	-1.22 ± 1.51
$4.00\times10^{-3} - 1.25\times10^{-2}$	8.30×10^{-3}	47223	3.11 ± 1.09	0.11 ± 0.58
$1.25\times10^{-2} - 2.25\times10^{-2}$	1.75×10^{-2}	55473	2.62 ± 1.01	1.23 ± 0.52
$2.25\times10^{-2} - 3.25\times10^{-2}$	2.73×10^{-2}	49386	3.17 ± 1.07	-0.35 ± 0.57
$3.25\times10^{-2} - 4.25\times10^{-2}$	3.68×10^{-2}	29852	2.17 ± 1.39	-0.21 ± 0.61
$4.25\times10^{-2} - 5.00\times10^{-2}$	4.75×10^{-2}	9563	0.27 ± 2.77	0.35 ± 1.29

$$\epsilon_{\uparrow/\downarrow} = \frac{\sqrt{N(L,+,\uparrow/\downarrow)N(R,-,\uparrow/\downarrow)} - \sqrt{N(L,-,\uparrow/\downarrow)N(R,+,\uparrow/\downarrow)}}{\sqrt{N(L,+,\uparrow/\downarrow)N(R,-,\uparrow/\downarrow)} + \sqrt{N(L,-,\uparrow/\downarrow)N(R,+,\uparrow/\downarrow)}}, \tag{27}$$

$$\epsilon_{+/-} = \frac{\sqrt{N(L,+/-,\uparrow)N(R,+/-,\downarrow)} - \sqrt{N(L,+/-,\downarrow)N(R,+/-,\uparrow)}}{\sqrt{N(L,+/-,\uparrow)N(R,+/-,\downarrow)} + \sqrt{N(L,+/-,\downarrow)N(R,+/-,\uparrow)}}. \tag{28}$$

The six raw asymmetries that are described above are used as a check of the systematic errors. The differences $\Delta\epsilon_{LR} = \epsilon_L - \epsilon_R$ (*space* asymmetry), $\Delta\epsilon_{\uparrow\downarrow} = \epsilon_\uparrow - \epsilon_\downarrow$ (*snake* asymmetry), and $\Delta\epsilon_{+-} = \epsilon_+ - \epsilon_-$ (*tagging* asymmetry) should all be consistent with zero.

VI. RESULTS AND DISCUSSIONS

The analyzing power A_N in *pp* elastic scattering was measured using the 200-GeV/*c* polarized proton beam facility at the Fermi National Accelerator Laboratory (Fermilab) for the first time in the Coulomb-nuclear region. The effective four-momentum transfer squared ranged from $1.5 \times 10^{-3}\,(\mathrm{GeV}/c)^2$ to $5.0 \times 10^{-2}\,(\mathrm{GeV}/c)^2$. The results are summarized in Table II, and Fig. 8 presents both the results and our earlier preliminary measurement at 185 GeV/*c* [24]. The asymmetry expected for pure interference of ϕ_5^e and $(\phi_1 + \phi_3)^h$ in *pp* scattering is represented with the solid line in Fig. 8. The errors shown in Table II are statistical only.

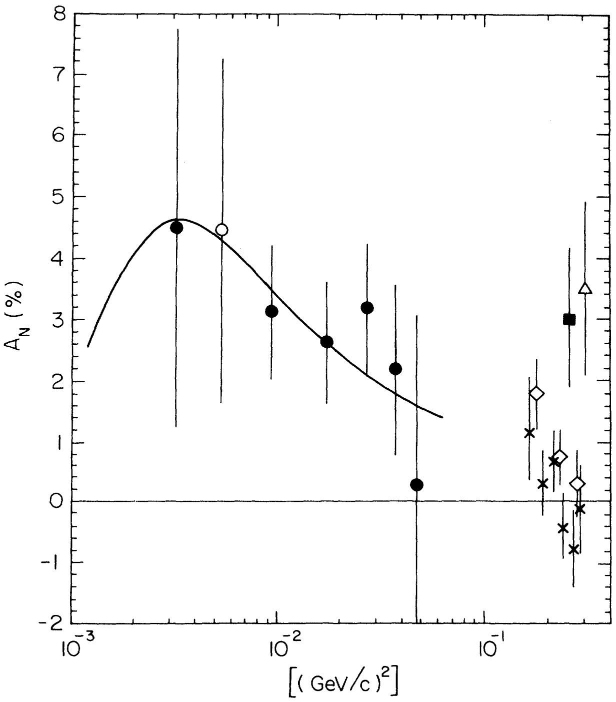

FIG. 8. A_N data for *pp* elastic scattering as a function of $-t$. The solid curve is the theoretical prediction [2] in the Coulomb-nuclear interference region. ○ is measured at 185 GeV/*c* [24] and the results of this measurement are indicated by ●. The other data points are measured at 300 GeV/*c* (cross) and 100 GeV/*c* (diamond) [16], 176 ± 12 GeV/*c* (triangle) [17], and at 150 GeV/*c* (black square) [15], using a polarized target.

For $-t > 0.004\,(\mathrm{GeV}/c)^2$, the background events, mainly from *p*C scattering and noninteracting beam particles, were successfully rejected by our trigger; for $-t \leq 0.004\,(\mathrm{GeV}/c)^2$, however, the error bar is large due to restrictive cuts to eliminate much of the background. We expect that noninteracting particles might dilute the measured asymmetry, but for *p*C scattering the analyzing power should be comparable to that of *pp* [25].

In order to verify that systematic uncertainties do not effect the asymmetry measurement, we give the measured raw asymmetry parameter $\epsilon(\langle P_b\rangle = 0)$ with the average-zero polarization part of the beam in Table II and in Table III we present the three *fake* asymmetry parameters as discussed in the previous section; $\Delta\epsilon_{LR}$, $\Delta\epsilon_{\uparrow\downarrow}$, and $\Delta\epsilon_{+-}$. They are all consistent with zero within statistical uncertainty.

For the sake of completeness, we include in Fig. 8 the polarization asymmetry results of previous *pp* elastic-scattering measurements performed at moderately low $-t$ values $[0.15 < -t < 0.3\,(\mathrm{GeV}/c)^2]$ at 100–300 GeV/*c* beam momenta [15–18]. They all used polarized targets as opposed to a polarized beam, as in our case. When these and other lower-energy experiments [27,28] are considered together over the full $-t$ range, they show the following general features for the asymmetry in *pp* elastic scattering at high energy.

(i) A positive analyzing power A_N at small $-t$ values $[-t < 0.3\,(\mathrm{GeV}/c)^2]$, decreasing with increasing s up to $s \approx 50\,(\mathrm{GeV})^2$, with possible flattening around values of a few percent up to the highest energies.

(ii) For $s > 50\,(\mathrm{GeV})^2$, A_N changes sign in the $-t$ range between 0.4 and 1.0 $(\mathrm{GeV}/c)^2$ and remains negative in the region where the diffractive dip in the differential cross section develops around $-t \approx 1.2\ (\mathrm{GeV}/c)^2$.

These features have stimulated a number of speculations on a possible hadronic spin-flip contribution ϕ_5^h that does not necessarily decrease as $\sqrt{s}$. It was suggested that diffractive scattering with the exchange of two pions could become important at large s; this mechanism can cause a nonvanishing ϕ_5^h because one of the two pions can couple with spin flip, while the other does not. More recently, it was pointed out that ϕ_5^h might remain nonzero at high energies if the nucleon contains a dynamically enhanced component with a compact diquark [14]. In the first case, the ratio of $\phi_5'^h$ (the reduced spin-flip amplitude corresponding to ϕ_5^h without the kinematical factor $\sqrt{t}$) and $(\phi_1 + \phi_3)^h$ can be as high as 0.25; in the second case, the effect is expected to be 0.05–0.1.

An attempt has been made to extract the behavior of $\phi_5'^h$ from cross-section and polarization data and the

TABLE III. The raw control asymmetries (*space, snake*, and *tagging*) for the CNI measurement. All the errors are statistical.

$-t$ range $(\mathrm{GeV}/c)^2$	$\Delta\epsilon_{LR}$ (%)	$\Delta\epsilon_{\uparrow\downarrow}$ (%)	$\Delta\epsilon_{+-}$ (%)
$1.50\times10^{-3}-4.00\times10^{-3}$	-3.74 ± 2.66	-0.45 ± 2.66	-2.12 ± 2.66
$4.00\times10^{-3}-1.25\times10^{-2}$	-1.04 ± 0.92	1.11 ± 0.92	-1.88 ± 0.92
$1.25\times10^{-2}-2.25\times10^{-2}$	0.64 ± 0.85	1.34 ± 0.85	-0.39 ± 0.85
$2.25\times10^{-2}-3.25\times10^{-2}$	-0.44 ± 0.90	0.24 ± 0.90	-2.19 ± 0.90
$3.25\times10^{-2}-4.25\times10^{-2}$	1.75 ± 1.17	1.39 ± 1.17	-0.05 ± 1.17
$4.25\times10^{-2}-5.00\times10^{-2}$	0.49 ± 2.33	-0.82 ± 2.33	4.15 ± 2.33

result is $\phi_5'^h$ might be comparable to $(\phi_1+\phi_3)^h$ at $-t=0$ [26]. It should be noted however that the observed polarization is dominated by the kinematical terms at relatively small $-t$ values and the data available at that time were limited to $|t|\geq0.15\,(\mathrm{GeV}/c)^2$.

The results presented here agree well with the theoretical prediction of a purely CNI asymmetry originating from the interference of ϕ_5^e and $(\phi_1+\phi_3)^h$ in the $-t$ range 10^{-3}–$10^{-2}\,(\mathrm{GeV}/c)^2$. Within experimental accuracy, the results do not discount the possibility of a nonzero spin-flip hadronic amplitude at the level of a few percent of the dominating nonflip one. There is no measurement of analyzing power to this day in the range $0.05\leq-t\leq0.15\,(\mathrm{GeV}/c)^2$. In view of the renewed interest in the high-energy behavior of elastic scattering and the debated structure of the Pomeron, it might be of significant interest to extend these types of measurements with high precision to the range of $0.001\leq-t\leq0.2\,(\mathrm{GeV}/c)^2$.

ACKNOWLEDGMENTS

The authors would like to acknowledge the assistance of the Fermilab Research Division, as well as the support of the technical personnel in the home institutions of the participating groups. In particular we would like to acknowledge the help of P. Ciliberti, G. Menon, and G. Vernier for the design and construction of most of the proportional wire chambers used in this experiment; S. Reia, R. Stoicovich, E. Clemmens, and E. Ruth for the construction of mechanical parts and assembly; and C. Boneschi, M. Gregori, G. Kidric, and F. Tommasini for the design and installation of MSD and MST electronics. This work would not have been possible without the ideas and efforts of our colleagues M. M. Gazzaly, R. Rzaev, N. Tanaka, and A. Villari, as well as the generous technical support of F. Pucci; we regret their passing away and we will miss them all greatly. Work for this project is supported by the U.S. Department of Energy, Division of High Energy Physics, Contracts Nos. W-31-109-ENG-38, DE-AC02-76CH03000, DE-AC02-76ER02289, W-7405-ENG-36, DE-AS05-76ER05096, and DE-FG02-91ER40664; the Istituto Nationale di Fisica Nucleare (INFN), Italy; the USSR State Committee on Utilization of Atomic Energy (SCUAE); the Commisariat à l'Energie Atomique, France; the Ministry of Science, Culture and Education in Japan; and LAPP-IN2P3, Annecy-le-Vieux, France.

---

[1] J. Schwinger, Phys. Rev. **69**, 681 (1946).
[2] B. Z. Kopeliovich and L. I. Lapidus, Yad. Fiz. **19**, 218 (1974) [Sov. J. Nucl. Phys. **19**, 114 (1974)].
[3] N. H. Buttimore, E. Gotsman, and E. Leader, Phys. Rev. D **18**, 694 (1978).
[4] L. D. Solov'ev, Zh. Eksp. Teor. Fiz. **49**, 292 (1965) [Sov. Phys. JETP **22**, 205 (1966)].
[5] A. Garren, Phys. Rev. **101**, 419 (1956).
[6] M. Jacob and G. C. Wick, Ann. Phys. (N.Y.) **7**, 404 (1959).
[7] J. Bystricky, F. Lehar, and P. Winternitz, J. Phys. (Paris) **39**, 1 (1978).
[8] L. G. Ratner, Czech. J. Phys. B **26**, 34 (1976).
[9] L. Fajardo-Paz, Ph.D. thesis, 1980 (unpublished).
[10] A. Schiz *et al.*, Phys. Rev. D **21**, 3010 (1980).
[11] J. P. Burq *et al.*, Nucl. Phys. **B217**, 285 (1983).
[12] D. Bernard *et al.*, Phys. Lett. B **198**, 583 (1987).
[13] N. Amos *et al.*, Phys. Lett. B **247**, 127 (1990).
[14] B. Z. Kopeliovich and B. G. Zakharov, Phys. Lett. B **226**, 156 (1989).
[15] G. Fidecaro *et al.*, Phys. Lett. **76B**, 369 (1978); G. Fidecaro *et al.*, *ibid.* **105B**, 309 (1981).
[16] J. H. Snyder *et al.*, Phys. Rev. Lett. **41**, 781 (1978).
[17] M. Corcoran *et al.*, Phys. Rev. D **22**, 2624 (1980).
[18] R. V. Kline *et al.*, Phys. Rev. D **22**, 553 (1980).
[19] D. P. Grosnick *et al.*, Nucl. Instrum. Methods A **290**, 269 (1990).
[20] L. M. Bollinger and G. E. Thomas, Rev. Sci. Instrum. **32**, 1044 (1961).
[21] F. T. Kuchnir and F. J. Lynch, IEEE Trans. Nucl. Sci. **NS-15**, 107 (1968).
[22] M. Arignon *et al.*, Nucl. Instrum Methods A **235**, 523 (1985). The hodoscope described here is a circular one, whereas the Gray Code hodoscope used for CNI measurement has a rectangular geometry. The underlying principles of operations, though, are identical.
[23] W. H. Barkas and M. J. Berger, *Tables of Energy Losses and Ranges of Heavy Charged Particles* (NASA Report No. SP-3013, Washington, D.C., 1964).
[24] N. Akchurin *et al.*, Phys. Lett. **29B**, 299 (1989).
[25] N. H. Buttimore, in *High Energy Spin Physics (Brookhaven National Laboratory and Westhampton Beach, New York)*, Proceedings of the Fifth High Energy Spin Symposium, edited by G. M. Bunce, AIP Conf. Proc. No. 95 (AIP, New York, 1983), p. 634.
[26] K. Hinotani *et al.*, Nuovo Cimento A **52**, 363 (1979).
[27] A. Gaidot *et al.*, Phys. Lett. **61B**, 103 (1976).
[28] F. Lehar *et al.*, Europhys. Lett. **3**, 1175 (1987).